The Astrophysical Journal, 943:89 (10pp), 2023 February 1 https://doi.org/10.3847/1538-4357/acaaa0
© 2023. The Author(s). Published by the American Astronomical Society.
OPEN ACCESS

A Study of Particle Transport in Young Pulsar Wind Nebulae

Bo-Tao Zhu[1,2], Fang-Wu Lu[2,3], and Li Zhang[2]
[1] College of Science, Yunnan Agricultural University, Kunming, 650201, People's Republic of China
[2] Department of Astronomy, Key Laboratory of Astroparticle Physics of Yunnan Province, Yunnan University, Kunming, 650091, People's Republic of China
lizhang@ynu.edu.cn
[3] Department of Physics, Yuxi Normal University, Yuxi, 653100, People's Republic of China
Received 2022 March 20; revised 2022 December 5; accepted 2022 December 7; published 2023 January 27

Abstract

The broadband emission of numerous pulsar wind nebula (PWNe) in our Galaxy can be well described by synchrotron radiation and inverse Compton scattering from relativistic particles, specifically electrons and positrons. However, the particle transport mechanism is still under debate. We use here a time-dependent model to investigate the particle transport process of the young PWN, while the particle cooling processes are also analyzed. Following applications of the model to six young PWNe, our results show that (1) the particle cooling process is dominated by adiabatic loss in the low-energy band but by synchrotron loss in the high-energy band; (2) the advection dominates the particle transport process in the low-energy band, whereas the advection and diffusion codominate in the high-energy band, indicating that both advection and diffusion play an important role in particle transport; and (3) the diffusion coefficient is (2–360) $\times$ 10^{24} cm^2 s^{-1} at the electron energy of 1 TeV, i.e., about 3 orders of magnitude smaller than the value considered to be the average in the Galaxy. We conclude that a slow-diffusion mechanism may explain the multiband observation of the sample of six young PWNe considered in this study.

Unified Astronomy Thesaurus concepts: Pulsars (1306); Pulsar wind nebulae (2215); Supernova remnants (1667)

1. Introduction

A pulsar wind nebula (PWN) is a bubble of magnetized relativistic particles (electrons and positrons) and is created by the interaction of the pulsar wind with the surrounding ambient medium, either the supernova (SN) ejecta or the interstellar medium (e.g., Rees & Gunn 1974; Kennel & Coroniti 1984; Gaensler & Slane 2006; Slane 2017). The pulsar wind is accelerated at the terminal shock and injected into the PWN, and the accelerated relativistic particles can emit nonthermal photons from radio to PeV gamma-ray bands (e.g., Reynolds et al. 2017; Driessen et al. 2018; Cao et al. 2021a, 2021b). Given the particle transport, the radiation zone typically extends to distances of tens of parsecs. Currently, about 40 extended TeV sources associated with pulsars are firmly identified by various nonthermal photon observations (for details, see http://tevcat2.uchicago.edu/). These observed photon spectra of PWNe give us some important information for studying the nonthermal radiation properties of high-energy particles, such as acceleration, diffusion, and advection.

Theoretically, to explain the observed multiband nonthermal photon spectral energy distributions (SEDs), some pure leptonic models have been proposed (e.g., Kennel & Coroniti 1984; De Jager et al. 2008; Zhang et al. 2008; Gelfand et al. 2009; Fang & Zhang 2010; Tanaka & Takahara 2010; Bucciantini et al. 2011; Martin et al. 2012; Torres et al. 2014; Torres & Lin 2018; Zhu et al. 2018; Fiori et al. 2020; Zhu et al. 2021). In these models, two different particle populations are required. Some particles are accelerated in the light cylinder of the pulsar or reconnecting current sheets of the bulk of the nebula (e.g., Atoyan & Aharonian 1996; Lyutikov et al. 2019). Other particles are considered to be accelerated at the pulsar wind termination shock of the equatorial portion (e.g., Rees & Gunn 1974; Kennel & Coroniti 1984). Meanwhile, the radio to X-ray band photons are generally believed to be produced by the synchrotron radiation, and GeV to TeV gamma-rays are produced via inverse Compton (IC) scattering of ultrarelativistic electrons and positrons. However, the latter is also produced via the decay of neutral pions in the proton–proton interaction of energetic nucleons with the ambient interstellar medium. Hence, a possible hadronic origin has been suggested as an alternative or an additional component to IC scattering gamma-rays (e.g., Cheng et al. 1990; Atoyan & Aharonian 1996; Horns et al. 2006; Yang & Zhang 2009; Zhang & Yang 2009; Li et al. 2010).

There are two prominent mechanisms that have been invoked to explain particle transport within PWNe: advection and diffusion. The pure diffusion model was first proposed to investigate the characteristics of a PWN (e.g., Gratton 1972; Wilson & Shakeshaft 1972), and the pure advection model has also been proposed (e.g., Rees & Gunn 1974; Kennel & Coroniti 1984). In fact, it is likely that advection and diffusion play an important role in the particle transport process (e.g., Van Etten & Romani 2011; Tang & Chevalier 2012; Vorster & Moraal 2013; Porth et al. 2016; Lu et al. 2017a, 2017b; Ishizaki et al. 2018; van Rensburg et al. 2018; Lu et al. 2019, 2020; van Rensburg et al. 2020). However, it is still controversial whether the particle transport process is governed by advection or diffusion. Some studies suggest that convection dominates particle propagation (e.g., H.E.S.S. Collaboration 2019; Lu et al. 2020), while other studies suggest that diffusion is the dominant particle transport process (e.g., Abeysekara et al. 2017; Liu & Yan 2020).

Additionally, some investigations revealed that the particle diffusion process within PWNe is significantly slow compared to the average of the interstellar medium in the Galaxy

Original content from this work may be used under the terms of the Creative Commons Attribution 4.0 licence. Any further distribution of this work must maintain attribution to the author(s) and the title of the work, journal citation and DOI.

(e.g., Wilson & Shakeshaft 1972; Lu et al. 2017a, 2019, 2020; Hu et al. 2022). Furthermore, HAWC, Milagro, Fermi-LAT, and LHAASO found numerous extended gamma-ray sources around middle-aged pulsars (10 kyr), which have been named "TeV halos" or "gamma-ray halos" (e.g., Linden et al. 2017; Di Mauro et al. 2019), and whose observation information also suggested that the particle diffusion is inhibited in the halo region (e.g., Aharonian et al. 2005c; Abeysekara et al. 2017; Di Mauro et al. 2020; Bao et al. 2022). These studies indicated that the high-energy particle diffusion is slower in the vicinity of these pulsars than it is elsewhere in the interstellar medium, whereas other studies suggested that the gamma-ray halos may also be explained without a slow-diffusion environment (e.g., Liu et al. 2019; Recchia et al. 2021). Motivated by these studies, in order to research the particle transport processes within PWNe, a spatially independent spectral evolution model with particle advection and diffusion was constructed in our previous work (e.g., Zhu et al. 2021), and the model has been applied to the Crab Nebula, 3C 58, and G54.1+0.3, reproducing the current observed spectrum. The result showed that the particle transport process is advection dominated and a slow-diffusion process occurs within the three PWNe.

In this paper, we use a spectral evolution model to investigate the particle advection and diffusion processes in additional PWNe observed at different energy bands. The structure is as follows. In Section 2, we briefly review the model. In Section 3, we apply the model to six PWNe and calculate the SEDs of each PWN. Finally, our conclusions and discussions are presented in Section 4.

2. Model Description

A PWN is powered by the center pulsar through its spin-down power, and the spin-down power of the pulsar with a period P, a period derivative $\dot{P}$, and a braking index n is given by (e.g., Gaensler & Slane 2006)

$$L(t) = L_0\left(1 + \frac{t}{\tau_0}\right)^{-\frac{n+1}{n-1}}, \tag{1}$$

where L_0 is the initial luminosity and τ_0 is the initial spin-down timescale. For a pure dipole radiative pulsar, $L(t)$ can be estimated by $L(t) = 4\pi^2 I\dot{P}/P^3$, where I is the pulsar moment of inertia. And then the initial luminosity, L_0, and initial spin-down timescale, τ_0, are given by

$$L_0 = L(t)\left(1 + \frac{t}{\tau_0}\right)^{\frac{n+1}{n-1}} \tag{2}$$

and

$$\tau_0 = \frac{2\tau_c}{n-1} - T_{\rm age}, \tag{3}$$

where τ_c is the characteristic age of the pulsar,

$$\tau_c = \frac{P}{2\dot{P}}, \tag{4}$$

and $T_{\rm age}$ is the age of the PWN. If I, $T_{\rm age}$ and n are given, the L_0 and τ_0 can be obtained.

In general, the majority of spin-down power is carried by the pulsar wind into PWNe (e.g., Rees & Gunn 1974; Kennel & Coroniti 1984) and distributed between particle energy ($\dot{E}_e(t) = \eta_e L(t)$) and the magnetic field energy ($\dot{E}_B = \eta_B L(t)$). Meanwhile, two different particle populations are required inside the nebula: a low-energy component, which has a power-law form with index <2.0, and a high-energy component, which has a power-law form with index >2.0. The former is accelerated in the light cylinder of the pulsar or reconnecting current sheets of the bulk of the nebula (e.g., Atoyan & Aharonian 1996; Lyutikov et al. 2019), and the latter is considered to be accelerated at the pulsar wind termination shock of the equatorial portion (e.g., Rees & Gunn 1974; Kennel & Coroniti 1984). Thus, the accelerated particles are assumed typically to be a broken power-law form

$$Q(E, t) = Q_0(t)\begin{cases}\left(\frac{E}{E_b}\right)^{-\alpha_1} & \text{for } E \leqslant E_b,\\ \left(\frac{E}{E_b}\right)^{-\alpha_2} & \text{for } E_b \leqslant E < E_{\rm max},\end{cases} \tag{5}$$

where $Q_0(t)$ is a time-dependent normalization coefficient, E_b is the break energy, and α_1 and α_2 are low- and high-energy spectral indices, respectively. Note that conventional models predict the break energy $E_b \sim 10^4$–10^6 MeV, but the corresponding physical mechanisms are still unclear (e.g., Bucciantini et al. 2011; Tanaka & Takahara 2011; Torres et al. 2014; Zhu et al. 2018). Generally, if the magnetic energy is completely transferred to the particles (either in the wind or at the terminal shock), the break energy is considered to be proportional to the bulk Lorentz factor γ_w and wind magnetization σ_w, that is, $E_b \sim \gamma_w \sigma_w m_{\pm e} c^2$ (e.g., Lyutikov et al. 2019; Luo et al. 2020). Although numerous studies have shown $\gamma_w \sim 10^2$–10^6 (e.g., Arons & Scharlemann 1979; Arons 2012; Torres et al. 2014; Zhu et al. 2018; Lyutikov et al. 2019), the change of magnetization is severe. Theoretical models of pulsar magnetospheres and wind predict $\sigma_w \gg 1$ (e.g., Arons 2012), whereas the simple 1D models of PWNe only require $\sigma_w \ll 1$ (e.g., Rees & Gunn 1974; Kennel & Coroniti 1984). The discrepancy is known as the σ-problem. Lastly, $E_{\rm max}$ is the maximum energy of the injected electrons and positrons, given by (e.g., Martin et al. 2012; Torres et al. 2014)

$$E_{\rm max} \approx k\epsilon e\sqrt{\frac{\eta_B L(t)}{c}}, \tag{6}$$

where ϵ is the ratio of the Larmor radius to the PWN radius. In order to confine the accelerated particles within the PWN, it is necessary for the radius of the PWN to be larger than the Larmor radius; thus, $0 < \epsilon < 1$ (e.g., Venter & de Jager 2007). For strong shocks, the magnetic compression ratio at the shock is about 3, and k is assumed to be 3 here (e.g., Holler et al. 2012). Then, the time-dependent normalization coefficient $Q_0(t)$ can be estimated by

$$(1 - \eta_B)L(t) = \int_0^{E_{\rm max}} Q(E, t)EdE, \tag{7}$$

where $(1 - \eta_B)L(t)$ is energy of electrons and positrons.

Assuming spherical symmetry, the particle transport equation within nebulae can be written as (e.g., Zhu et al. 2021)

$$\frac{\partial N(E, t)}{\partial t} = \frac{\partial}{\partial E}[\dot{E}N(E, t)] + \frac{N(E, t)}{\tau_{\rm con}(E, t)} + \frac{N(E, t)}{\tau_{\rm diff}(E, t)} + Q(E, t), \tag{8}$$

where an isotropic distribution of the electrons and positrons in the PWN is assumed. The particle cooling process includes the adiabatic losses $\dot{E}_{\rm ad}$, synchrotron radiation losses $\dot{E}_{\rm syn}$, and IC scattering losses $\dot{E}_{\rm IC}$. Thus, the energy-loss rate $\dot{E}$ is written as

$$\dot{E} = \dot{E}_{\rm ad} + \dot{E}_{\rm syn} + \dot{E}_{\rm IC}, \quad (9)$$

On the other hand, the transport process includes advection and diffusion. According to Zhu et al. (2021), the advection velocity can be approximated as

$$V(r) = V_{\rm PWN}(t)\left[\frac{R_{\rm PWN}(t)}{r}\right], \quad (10)$$

and the advection timescale of particles $\tau_{\rm con}$ is described as (e.g., Vorster & Moraal 2013)

$$\tau_{\rm con} = \int_{R_{\rm ts}}^{R_{\rm PWN}} \frac{1}{V(r)} dr. \quad (11)$$

Integrating Equation (11) from $R_{\rm ts}$ to $R_{\rm pwn}$, the $\tau_{\rm con}$ is written as

$$\tau_{\rm con} = \frac{1}{2}\left(\frac{R_{\rm pwn}}{V_{\rm pwn}} - \frac{R_{\rm ts}^2}{V_{\rm pwn}R_{\rm pwn}}\right) = \frac{1}{2}\tau_{\rm ad} - \frac{R_{\rm ts}^2}{2V_{\rm pwn}R_{\rm pwn}}, \quad (12)$$

where $R_{\rm ts}$ is the radius of the termination shock. Then, the diffusion coefficient is assumed to be (e.g., Zhu et al. 2021)

$$K(t) = \frac{K(t_{\rm ini})B_{\rm pwn}(t_{\rm ini})}{B_{\rm pwn}(t)}\left[\frac{E_e}{1{\rm TeV}}\right]^{\delta}, \quad (13)$$

where $K(t_{\rm ini})$ and $B_{\rm pwn}(t_{\rm ini})$ are the initial diffusion coefficient and initial magnetic field strength, respectively, and $t_{\rm ini}$ is the initial birth time of the pulsar. The diffusion coefficient increases with energy, that is, $\propto E^{\delta}$. Here the value of δ depends on the property of turbulence in the ambient medium, and the different values of δ represent different diffusion forms (e.g., Kolmogorov 1941; Strong et al. 2007; Trotta et al. 2011; Feng et al. 2016; López-Coto et al. 2022). For example, $\delta = 1/3$ represents a typical Kolmogorov turbulence diffusion, $\delta = 1/2$ represents a typical Kraichnan turbulence diffusion, and $\delta = 1$ represents a Bohm-like diffusion. In fact, the relativistic turbulence is very intricate in pulsar wind nebulae. According to Parker (1965), the diffusion timescale of particles $\tau_{\rm diff}$ is described by

$$\tau_{\rm diff} = \frac{R_{\rm pwn}^2(t)}{6K(t)}, \quad (14)$$

where $R_{\rm pwn}(t)$ is the radius of the PWN.

According to the conservation of magnetic energy, the average magnetic field in the nebula $B_{\rm PWN}(t)$ is calculated with (e.g., Gelfand et al. 2009; Zhu et al. 2018)

$$B_{\rm pwn}(t) = \left(\frac{1}{R_{\rm pwn}(t)}\right)^2 \sqrt{6\eta_B \int_0^t L(t')R_{\rm pwn}(t')dt'}. \quad (15)$$

To calculate the SED of nonthermal photons, the particle spectra at the current time ($N(E,t)$) is obtained by solving the transport equation of particles (Equation (8)), and then the SEDs of nonthermal photons are calculated through synchrotron radiation and IC scattering of relativistic electrons and positrons inside the PWN. For the synchrotron radiation, the emissivity is given by (e.g., Blumenthal & Gould 1970; Rybicki & Lightman 1979)

$$Q_{\rm syn}(E_\gamma, t) = \int_0^\infty N(E, t)P_{\rm syn}(E_\gamma, E, B_{\rm pwn}(t))dE, \quad (16)$$

where $P_{\rm syn}(E_\gamma, E, B_{\rm pwn}(t))$ is the power emitted by a single relativistic electron, which is expressed as

$$P_{\rm syn}(E_\gamma, E, B_{\rm pwn}(t)) = \frac{\sqrt{3}e^3 B_{\rm pwn}(t)}{m_e c^2}F\left(\frac{E_\gamma}{E_c}\right), \quad (17)$$

where E_c is the critical energy, $F(x) = x\int_x^\infty K_{5/3}(y)dy$ with $x = E_\gamma/E_c$, and $K_{5/3}(y)$ is the modified Bessel function of order 5/3.

The emission coefficient of the IC scattering can be expressed as (e.g., Jones 1968; Blumenthal & Gould 1970)

$$Q_{\rm ics}(E_\gamma, t) = \int_0^\infty N(E, t)P_{\rm ics}(E, E_\gamma, t)dE, \quad (18)$$

where $P_{\rm ics}(E_\gamma, E, t)$ is the scattered photon spectrum per electron, which is given by

$$P_{\rm ics}(E, E_\gamma, t) = \frac{3}{4}\frac{\sigma_T c}{(E/m_e c^2)^2}\int_0^\infty \frac{n(\epsilon_i)}{\epsilon_i} f(q, \Gamma_\epsilon)d\epsilon_i, \quad (19)$$

where ϵ_i is the target photon energy and $n(\epsilon_i)$ is the distribution of the target photon fields. The function $f(q, \Gamma_\epsilon)$ can be expressed as (e.g., Jones 1968; Blumenthal & Gould 1970)

$$f(q, \Gamma_\varepsilon) = 2q\ln q + (1-q)\left((1+2q) + \frac{1}{2}\frac{(\Gamma_\epsilon q)^2}{1+\Gamma_\epsilon q}\right), \quad (20)$$

with $\Gamma_\epsilon = 4\epsilon(E/m_e c^2)/m_e c^2$ and $q = E_\gamma/\Gamma_\epsilon(E - E_\gamma)$. In the calculation processes, target photons consist of four components, the cosmic microwave background (CMB) photons, the galactic near-infrared (NIR) photons, the far-infrared (FIR) photons, and synchrotron self-Compton (SSC) radiation photons. The energy density and temperature of the CMB photons are $U_{\rm CMB} = 0.25\,{\rm eV\ cm^{-3}}$ and $T_{\rm CMB} = 2.7$ K, respectively. Since the interstellar radiation field of GALPROP is not uniform in space, the energy densities ($U_{\rm FIR}$, $U_{\rm NIR}$) and temperatures ($T_{\rm FIR}$, $T_{\rm NIR}$) could be different for different positions of the PWN source.

Similar to Gelfand et al. (2009), the dynamical properties can be self-consistently studied for the PWN. As mentioned in Gelfand et al. (2009), the large-scale evolution of a composite supernova remnant (SNR) depends on the mechanical energy of the explosion $E_{\rm sn}$, the density of the ambient medium $\rho_{\rm ISM}$, the mass of the SN ejecta $M_{\rm ej}$, and the spin-down power of the pulsar $L(t)$. The time evolutions of the SNR radius $R_{\rm snr}(t)$, the reverse shock radius $R_{\rm rs}(t)$, the PWN radius $R_{\rm PWN}(t)$, and the termination shock radius $R_{\rm ts}(t)$ of the PWN can be calculated. The calculation process here is the same as in Gelfand et al. (2009) (for details, see their Section 2.2 or Appendix A of Zhu et al. 2018).

3. Applications

Here, to investigate the nonthermal radiation properties of PWNe, we apply the model to six PWNe: G21.5–0.9, Kes 75, G0.9+0.1, MSH 15–52, N157B, and HESS J1356–645. We choose these PWNe according to two criteria: (1) the period and period derivative of central pulsar in each PWN are known,

Table 1
Physical Parameters Used for PWNe in This Study

PWN	G21.5–0.9	KES 75	G0.9+0.1	N157B	MSH 15–52	HESS J1356–645
			Pulsar and Ejecta Parameters			
P (ms)	61.8	324.0	52.2	16.12	150	166
$\dot{P}$ (s s^{-1})	2.02×10^{-13}	7.08×10^{-12}	1.56×10^{-13}	5.13×10^{-14}	1.50×10^{-12}	3.6×10^{-13}
n	3.0	2.19	3.0	3.0	1.4	3.0
d (kpc)	4.1	5.8	13.3	53.7	4.4	2.5
τ_c (yr)	4850	726	5305	4982	1585	7310
$T_{\rm age}$ (yr)	900	1000	3000	4600	4000	6500
$L(t)$ (erg s^{-1})	6.76×10^{37}	1.64×10^{37}	1.30×10^{38}	1.21×10^{39}	3.50×10^{37}	6.20×10^{36}
L_0 (erg s^{-1})	1.02×10^{38}	1.62×10^{39}	6.86×10^{38}	2.05×10^{41}	2.36×10^{39}	5.04×10^{38}
τ_0 (yr)	3950	220	2305	382	3927	810
$M_{\rm ej}$ ($M_\odot$)	8.0	10.0	13.0	23.0	6.0	8.0
$E_{\rm SN}$ (10^{51} erg)	1.0	1.0	1.0	1.0	1.0	1.0
$n_{\rm H}$ (cm^3)	0.1	0.1	0.01	0.01	0.01	0.05
			Target Photon Parameters			
$T_{\rm FIR}$ (K)	35.0	25.0	51.0	88.0	30.0	25.0
$U_{\rm FIR}$ (eV cm^{-3})	1.4	2.5	9.4	8.9	1.2	2.5
$T_{\rm NIR}$ (K)	3500.0	5000.0	5889.0	80.0	400.0	5000.0
$U_{\rm NIR}$ (eV cm^{-3})	5.0	1.4	29.2	2.7	20.0	1.2
			Fitted Parameters			
E_b (10^5 MeV)	0.56 ± 0.15	8.26 ± 4.21	0.23 ± 0.21	0.65 ± 0.17	0.50 ± 2.78	0.54 ± 0.47
α_1	1.12 ± 0.17	1.73 ± 0.10	1.12 ± 0.72	1.36 ± 0.09	1.26 ± 2.81	1.00 ± 0.30
α_2	2.69 ± 0.02	2.56 ± 0.03	2.63 ± 0.09	2.68 ± 0.03	2.36 ± 0.11	2.56 ± 0.12
η_B	0.020 ± 0.005	0.0029 ± 0.0003	0.010 ± 0.004	0.017 ± 0.002	0.20 ± 0.09	0.088 ± 0.04
ϵ	0.29 ± 0.38	0.82 ± 0.65	0.27 ± 1.73	0.16 ± 0.35	0.33 ± 0.63	0.37 ± 1.75
$K(t_{\rm ini})$ (10^{20} cm^2 s^{-1})	4.82 ± 9.55	3.21 ± 2.20	6.11 ± 14.96	5.12 ± 4.31	33.08 ± 36.43	8.46 ± 14.41
Reduced χ^2	1.12	2.12	0.46	2.87	0.65	1.11

Note. We report in each column the values for each source. The first section of the table contains the values of observed and calculated pulsar parameters and values of ejecta parameters used here, the second section contains the values of target photon parameters for IC scattering, the third section contains the fitted parameters together with fit errors, and the fourth section contains the values of reduced χ^2 obtained from the fit to the data.

and (2) nonthermal emissions at radio, X-ray, and TeV bands are accurately observed. Note that the particle transport (diffusion and advection) processes are still controversial within PWNe. It is generally assumed that the turbulence types of ambient medium are different for different stages of the evolution of PWNe, and the different turbulence may result in the different particle transport processes. In this paper, we considered only the free expansion stage. Meanwhile, the particle diffusion is assumed as a Kolmogorov diffusion, e.g., $\kappa(t) \sim Ee^{1/3}$ (e.g., Abeysekara et al. 2017; Tang & Piran 2019; Zhu et al. 2021), and the particle advection velocity $V(r) \sim 1/r$ within PWNe at the stage. For these sources, some of them may perhaps be beyond reverberation (e.g., Giacinti et al. 2020; López-Coto et al. 2022); if so, our model is just a simplification of the stages of the nebula evolution.

Using the model described in Section 2, the observed SEDs of nonthermal photons are reproduced well. To fit the observed SEDs for each PWN, pulsar and SN parameters and soft photon parameters are fixed. These parameter values are generally measured or assumed, and the corresponding values are listed in Table 1. In addition, the spectral parameters E_b, α_1, and α_2; the magnetic fraction η_B; the ratio of the Larmor radius to the PWN radius ϵ; and the initial diffusion coefficient $K(t_{\rm ini})$ are considered as fitted parameters. In the process, the Levenberg–Marquardt (LM) method of the χ^2 minimization fitting procedure (e.g., Press et al. 1992) is used to obtain the best-fitting values and their uncertainties. These values and reduced χ^2 values are also reported in Table 1. Note that, given the relatively poor data quality of our sample, some fitted parameter uncertainties are large. For comparison, the calculated SEDs and observed data of the PWN sample are shown in Figure 1. Meanwhile, the particle cooling and transport processes are analyzed. Detailed observations and calculation results are as follows.

1. *G21.5–0.9.*—The center pulsar is PSR J1833–1034 with a 61.8 ms rotation period, a period derivative of 2.02×10^{-13} s s^{-1}, and an assumed braking index of 3.0 (e.g., Camilo et al. 2006). The distance of 4.1 kpc is applied for the system (e.g., Abdalla et al. 2018). According to the observation of the expansion rate of the PWN, the age of G21.5–0.9 is estimated as $T_{\rm age} = 900$ yr (e.g., Bietenholz & Bartel 2008). For the age, the initial spin-down timescale $\tau_0 = 3950$ yr and the initial luminosity $L_0 = 1.02 \times 10^{38}$ erg s^{-1} are applied here.

The observed data are taken from Salter et al. (1989) (radio band); Gallant & Tuffs (1998) (IR band); De Rosa et al. (2009), Tsujimoto et al. (2011), and Nynka et al. (2014) (X-ray band); and Djannati-Atai et al. (2008) (gamma-ray band) for G21.5–0.9. The X-ray band images have revealed the angular radius $\theta_{\rm X-ray} \sim 40''$ (e.g., Matheson & Safi-Harb 2010; Hattori et al. 2020) and the corresponding radius $R_{\rm X-ray} \sim 0.8$ pc for

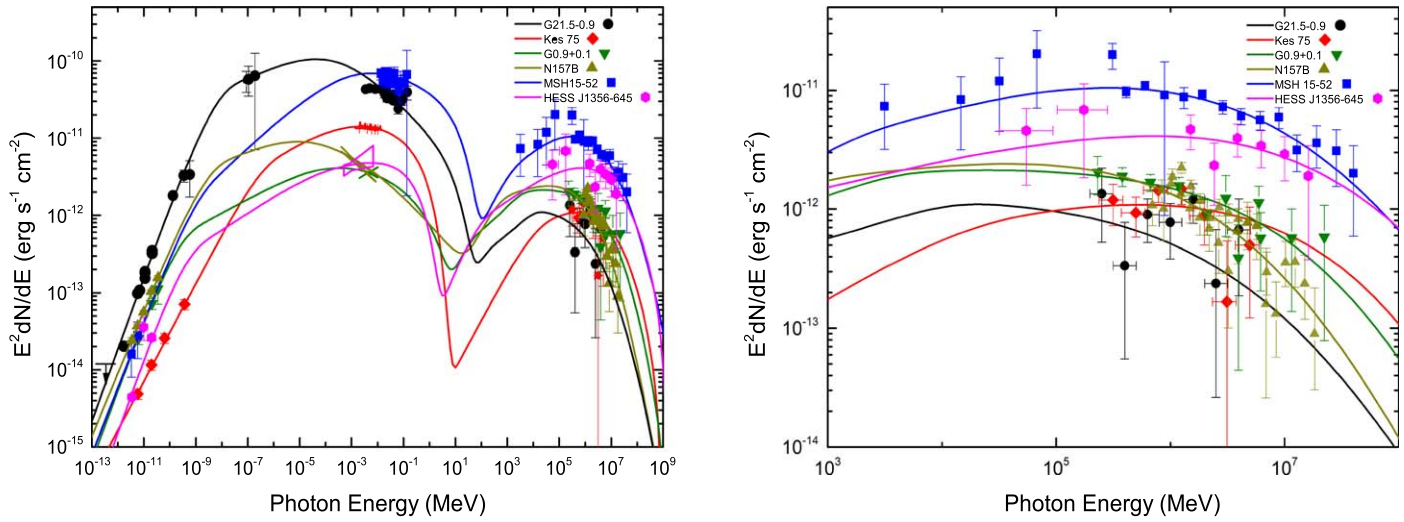

Figure 1. The left panel shows the comparison of calculated multiband SED with the observed data for six PWNe, and the right panel shows the comparison of the calculated SED with the observed data in the gamma-ray band. See text for detailed descriptions of the observed data.

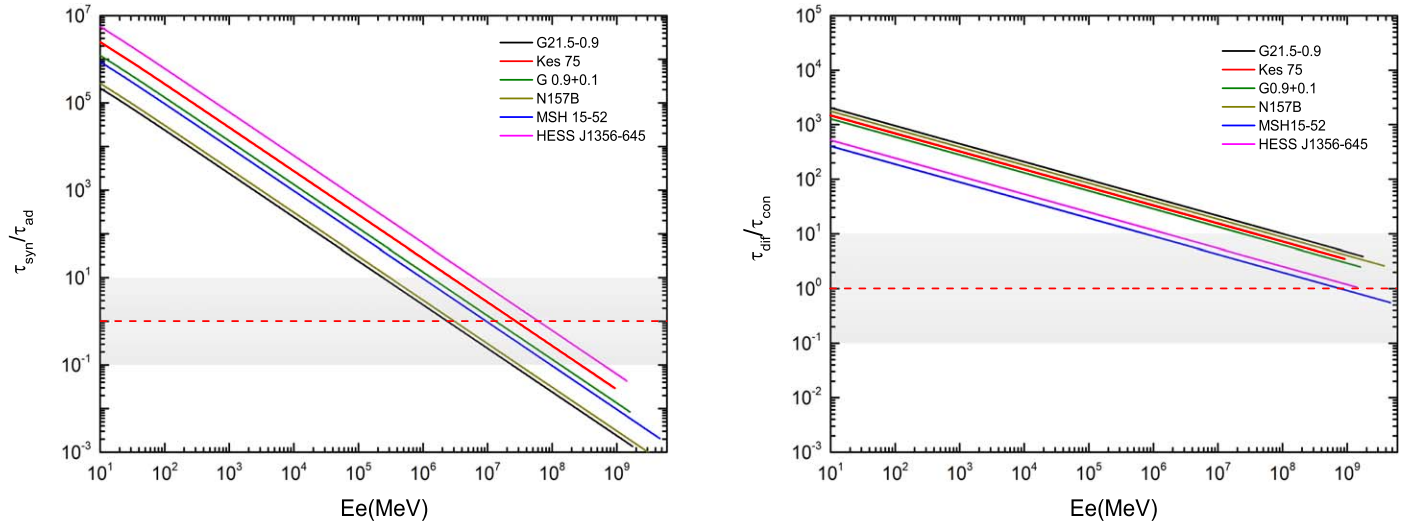

Figure 2. The left panel shows the ratio of $\tau_{\rm syn}/\tau_{\rm ad}$, whereas the right panel shows the ratio of $\tau_{\rm diff}/\tau_{\rm con}$. The red dotted lines represent the corresponding ratio $\tau_{\rm syn}/\tau_{\rm ad} = 1.0$ and $\tau_{\rm diff}/\tau_{\rm con} = 1.0$, respectively. The shaded band shows the ratio spanned in the range of 0.1–10.0.

the distance of 4.1 kpc. In addition, H.E.S.S. observations show the radius $R_{\rm TeV} < 4.0$ pc (e.g., Abdalla et al. 2018). As shown in Figure 1, the multiband observed data of G21.5–0.9 are reproduced well by synchrotron and IC emission of relativistic electrons and positrons, and the related parameters are listed in Table 1. From the modeling results, the low-energy spectral index has a value of $\alpha_1 \sim 1.12$, high-energy index is $\alpha_2 \sim 2.69$, and break energy is $E_b \sim 5.6 \times 10^4$ MeV, whereas from the model of Torres et al. (2014), we found that $\alpha_1 \sim 1.0$, $\alpha_2 \sim 2.5$, and $E_b \sim 5.11 \times 10^4$ MeV. Although these spectral parameters are not well consistent, they are very similar. In addition, to reproduce the observed gamma-ray SED, energy densities $U_{\rm IR} = 1.4$ eV cm^{-3} and $U_{\rm NIR} = 5.0$ eV cm^{-3} and temperatures $T_{\rm IR} = 35$ K and $T_{\rm NIR} = 3500$ K for the infrared and optical soft photons are used in the calculation. These values are consistent with the results obtained using the GALPROP code, which is based on the position of the source in the Galaxy (e.g., Porter et al. 2006). In fact, the same values are applied in Torres et al. (2014). By fitting the multiband observation data, our model shows a maximum energy of the electrons and positrons of ~1.8 PeV and a magnetic field strength of ~83.0 μG, which can compare with the magnetic field strength obtained by Torres et al. (2014), ~71.0 μG. In addition, our result gives $R = 0.83$ pc, which is consistent with the PWN-measured size in the X-ray band.

In addition, the particle cooling and transport processes are investigated in our model. The particle cooling process includes the adiabatic losses, synchrotron radiation losses, and IC scattering losses. However, the IC scattering loss effect is negligible. Thus, following Tang & Chevalier (2012), Porth et al. (2016), or Lu et al. (2020), the importance of adiabatic expansion relative to synchrotron loss and the importance of diffusion relative to advection are compared. The corresponding ratios of the timescales of these quantities are shown in Figure 2. The results show that the adiabatic loss is a prominent process for $E_e < 2.4 \times 10^6$ MeV, while the synchrotron cooling becomes the dominated process for $E_e > 2.4 \times 10^6$ MeV. On the other hand, the advection is the most prominent process to

particle transport within this nebula, and the diffusion only plays a role in the high-energy band. Meanwhile, our model predicted the current diffusion coefficient $\sim 2.1 \times 10^{24}$ cm^2 s^{-1} at the electron energy of 1 TeV, which is consistent with the result of the study of the spatially radiative properties (e.g., Lu et al. 2017b).

2. *Kes 75*.—The nebula is powered by PSR 1846–0258 with a rotational period $P = 324$ ms, a period derivative $\dot{P} = 7.08 \times 10^{-12}$ s s^{-1}, and a braking index $n = 2.19 \pm 0.03$ (e.g., Livingstone et al. 2006; Archibald et al. 2015). We assume a distance of 5.8 kpc to Kes 75 (e.g., Abdalla et al. 2018). Mereghetti et al. (2002), according to the pulsar timing observations, suggest that the true age of the remnant could be between 980 and 1700 yr. Here $T_{\rm age} = 1000$ yr. Consequently, the initial spin-down timescale $\tau_0 = 220$ yr and the initial luminosity $L_0 = 1.62 \times 10^{39}$ erg s^{-1} are used.

The multiband observed data are taken from Salter et al. (1989) and Bock & Gaensler (2005) (radio band), Gotthelf et al. (2021) (X-ray band), and Djannati-Atai et al. (2008) (gamma-ray band). The X-ray band observation shows that the angular radius $\theta_{\rm X-ray} = 30'' \pm 1\farcs7$ (e.g., Gotthelf et al. 2021), which indicates the corresponding radius $R_{\rm X-ray} = 0.84 \pm 0.05$ pc for the distance of 5.8 kpc. And the TeV size shows that $R_{\rm TeV} < 3.0$ pc (e.g., Abdalla et al. 2018). Using the parameters listed in Table 1, the multiband observed data are reproduced well, which is visible in Figure 1. In our model, the low-energy spectral index is $\alpha_1 \sim 1.73$, high-energy spectral index is $\alpha_2 \sim 2.56$, and break energy is $E_b \sim 8.3 \times 10^5$ MeV. These spectral parameter values are different from the $\alpha_1 \sim 1.4$, $\alpha_2 \sim 2.3$, and $E_b \sim 1.0 \times 10^5$ MeV of Torres et al. (2014). Contributing to this difference is likely the fact that in our model the newest X-band data (e.g., Gotthelf et al. 2021) are applied, whereas in the later model the X-ray band data are from Helfand et al. (2003). While, for the target photon energy densities and temperatures, the IR with $U_{\rm IR} = 2.5$ eV cm^{-3} and $T_{\rm IR} = 25$ K, and the NIR with $U_{\rm NIR} = 1.4$ eV cm^{-3} and $T_{\rm NIR} = 5000$ K are used (e.g., Torres et al. 2014). By fitting multiband observation data, the model predicted a maximum energy of the electrons and positrons of $\sim$0.93 PeV and a magnetic field strength of $\sim 22.0\,\mu$G, which are roughly consistent with the results of Torres et al. (2014). In addition, our model gives a radius of $\sim$1.0 pc, which is roughly consistent with the X-ray band observation results.

As shown in Figure 2, the particle cooling and transport processes are investigated. The results show that the adiabatic loss dominates the particle cooling process for $E_e < 2.7 \times 10^7$ MeV, while synchrotron loss dominates for $E_e > 2.7 \times 10^7$ MeV. Furthermore, advection is the most prominent transport process. Comparing with advection, diffusion is important only for the high-energy band. In addition, the current diffusion coefficient $\sim 3.62 \times 10^{24}$ cm^2 s^{-1} is obtained by the model. Very recently, Hu et al. (2022) applied a pure diffusion model to analyze the radial profiles of photon index and surface brightness and found diffusion coefficients of $\sim 5 \times 10^{25}$ cm^2 s^{-1}. Comparing with the modeling result derived from our model, the particle diffusion is relatively fast. The reason may be that the particle advection is considered and the particle diffusion is energy dependent in our model, but the particle advection is ignored and the particle diffusion is energy independent in Hu et al. (2022).

3. *G0.9+0.1*.—This is considered to be a young PWN, which is powered by pulsar PSR J1747−2809 with a rotation period of 52.2 ms and a period derivative of 1.56×10^{-13} s s^{-1} (e.g., Camilo et al. 2009). Since the braking index is unknown, $n = 3.0$ is assumed. The distance of the system is likely in the range from 8.0 to 16 kpc (e.g., Dubner et al. 2008); following Abdalla et al. (2018), we adopt a 13.3 kpc distance for the nebula. Camilo et al. (2009) estimated the age in the range between 2000 and 3000 yr. Here $T_{\rm age} = 3000$ yr. With the age, the initial spin-down timescale $\tau_0 = 2305$ yr and the initial luminosity $L_0 = 6.86 \times 10^{38}$ erg s^{-1} are applied.

The multiband observed data are taken from Dubner et al. (2008) (radio band), Porquet et al. (2003) (X-ray band), and Aharonian et al. (2005a) and Fiori et al. (2020) (TeV band). The observation shows that the angular radius of G0.9+0.1 is $1'$ in radio and X-ray bands (e.g., Helfand & Becker 1987; Sidoli et al. 2000; Porquet et al. 2003), which indicates the radius $R_{\rm X-ray} = 3.9$ pc, and the radius is smaller than 7 pc in the TeV band (e.g., Abdalla et al. 2018). Using the parameters listed in Table 1, the multiband observed data are reproduced well (see Figure 1). For the spectral parameters, corresponding values are as follows: $\alpha_1 \sim 1.12$, $\alpha_2 \sim 2.63$, and $E_b \sim 2.3 \times 10^4$ MeV, respectively. These results are roughly consistent with $\alpha_1 \sim 1.1$, $\alpha_2 \sim 2.53$, and $E_b \sim 4.5 \times 10^4$ MeV of Fiori et al. (2020). In addition, the target photon energy densities and temperatures, the IR with $U_{\rm IR} = 9.4$ eV cm^{-3} and $T_{\rm IR} = 51$ K and the NIR with $U_{\rm NIR} = 29.2$ eV cm^{-3} and $T_{\rm NIR} = 5889$ K, are applied (e.g., Fiori et al. 2020). By fitting the multi-band observation data, the results show a maximum energy of the electrons and positrons of $\sim$1.6 PeV and a magnetic field strength of $\sim 18.7\,\mu$G, which are consistent with Fiori et al. (2020). Meanwhile, the radius is $\sim$3.8 pc, which is consistent with the radio and X-ray band observation results.

For the particle transport, our results give the current diffusion coefficient $\sim 1.9 \times 10^{25}$ cm^2 s^{-1} at the electron energy of 1 TeV. Recently, van Rensburg (2018) applied a transport model including the advection and diffusion to spatially radiative properties of G0.9+0.1, whose result shows the diffusion coefficient $\sim 4.4 \times 10^{24}$ cm^2 s^{-1}. However, it should be noted that the particle diffusion is assumed to be Bohm-like diffusion, and the corresponding radius is set to be 2.5 pc in the model of van Rensburg (2018). Comparing with our model, these differences may result in a smaller diffusion coefficient. Meanwhile, as shown in Figure 2, we found that the particle cooling process is adiabatic loss dominated for $E_e < 1.3 \times 10^7$ MeV energy bands, while synchrotron loss dominates for $E_e > 1.3 \times 10^7$ energy bands. Furthermore, the advection dominates the transport process within the PWN.

4. *N157B*.—The center pulsar of N157B is PSR J0537−6910 (e.g., Marshall et al. 1998), which has a rotation period of 16.12 ms and a period derivative of $\dot{P} = 5.13 \times 10^{-14}$ s s^{-1} (e.g., Manchester et al. 2005). The braking index is unknown and assumed to be 3.0. The system has an estimated distance of 53.7 kpc (e.g., Abdalla et al. 2018). Here we assumed the age $T_{\rm age} = 4600$ yr, which is consistent with Martin et al. (2014). Hence, the initial spin-down timescale $\tau_0 = 382$ yr and initial luminosity $L_0 = 2.05 \times 10^{41}$ erg s^{-1} are used here.

The multiband observed data are taken from Lazendic et al. (2000) (radio band), Chen et al. (2006) (X-ray band), and Abramowski et al. (2012, 2015) (TeV band). The observation shows that the radiation dimension of PWN is 30×18 pc in radio band (e.g., Lazendic et al. 2000), which corresponds to a radius of a circle $R_{\rm radio} \sim 11.6$ pc for the distance of 53.7 kpc. The extended radiation region is not well defined in the TeV

band, and the corresponding radius $R_{\rm TeV} < 94$ pc is given by Abdalla et al. (2018). Using the parameters listed in Table 1, these observed data are reproduced well, and the results are shown in Figure 1. By the fitting process, the low-energy spectral index $\alpha_1 \sim 1.36$, high-energy index $\alpha_2 \sim 2.68$, and break energy $E_b \sim 6.5 \times 10^4$ MeV are obtained. The values can compare with Martin et al. (2014) given the $\alpha_1 \sim 1.5$, $\alpha_2 \sim 2.75$, and $E_b \sim 5.11 \times 10^5$ MeV and $\alpha_1 \sim 1.5$, $\alpha_2 \sim 2.6$, and $E_b \sim 1.02 \times 10^5$ MeV by considering ages of 4.6 and 2.5 kyr, respectively. For the IC scattering process, the upper-limit target photon energy densities and temperatures, IR with $U_{\rm IR} = 8.9$ eV cm^{-3} and $T_{\rm IR} = 88$ K and NIR with $U_{\rm NIR} = 2.7$ eV cm^{-3} and $T_{\rm NIR} = 80$ K (e.g., Indebetouw et al. 2009), are applied. The result implies a maximum energy of the electrons and positrons of ~3.7 PeV and a magnetic field strength of ~31.0 μG, which are roughly consistent with Martin et al. (2014), who obtained a magnetic field strength of ~35 μG by considering a lower age of 2.5 kyr to fit the TeV data. Meanwhile, the radius is ~10.3 pc, which is smaller than the result of radio observation. In fact, the shell is not well defined; it could include parts of the remnant (e.g., Lazendic et al. 2000).

For the particle transport process within this nebula, the current diffusion coefficient $\sim 6.3 \times 10^{25}$ cm^2 s^{-1} at the electron energy of 1 TeV is obtained by our model. In addition, from Figure 2 we found that the particle cooling process is adiabatic loss dominated for $E_e < 3.1 \times 10^6$ MeV energy bands, while synchrotron loss dominates for $E_e > 3.1 \times 10^6$ MeV energy bands. In addition, the advection is the most prominent process to particle transport.

5. *MSH 15−52*.—The nebula is powered by PSR B1509-58 with a rotational period $P = 150$ ms, a period derivative $\dot{P} = 1.5 \times 10^{-12}$ s s^{-1}, and a braking index $n = 2.839 \pm 0.003$ (e.g., Livingstone et al. 2005). The source is located at a distance of 5.2 ± 1.4 kpc (e.g., Gaensler et al. 1999); the distance of 4.4 kpc is adopted (e.g., Abdalla et al. 2018). We adopt $d = 4.4$ kpc throughout this paper. Following Zhu et al. (2018), the braking index $n = 1.4$ and the age $T_{\rm age} = 4000$ yr are applied. Thus, the initial spin-down timescale $\tau_0 = 3927$ yr and the initial luminosity $L_0 = 2.36 \times 10^{39}$ erg s^{-1} here.

The observed data are taken from Gaensler et al. (2002) (radio band), Mineo et al. (2001), Forot et al. (2006) (X-ray band), Abdo et al. (2010) (GeV band), and Aharonian et al. (2005b) (TeV band). In addition, the observations show that the average radius of the PWN $R_{\rm X-ray} = 10.2$ pc in X-ray (e.g., Forot et al. 2006; Giacinti et al. 2020) and $R_{\rm TeV} = 11.1 \pm 2.0$ pc in TeV bands (e.g., Abdalla et al. 2018). Figure 1 shows that the multiband observed data of MSH 15–52 are reproduced well, and the related parameters are listed in Table 1. From the modeling results, we found low-energy spectral index $\alpha_1 \sim 1.26$, high-energy index $\alpha_2 \sim 2.36$, and break energy $E_b \sim 5.0 \times 10^4$ MeV. However, it is worth noting that these values of the spectral parameters are not consistent with the values shown in previous studies (e.g., Torres et al. 2014; Lu et al. 2017a). In the model of Torres et al. (2014), $\alpha_1 \sim 1.5$, $\alpha_2 \sim 2.4$, and $E_b \sim 2.55 \times 10^5$ MeV. And $\alpha_1 \sim 1.65$, $\alpha_2 \sim 2.45$, and $E_b \sim 2.04 \times 10^5$ MeV for the model of Lu et al. (2017a). The main reason may be that the size of radiation regions is different. For the IC scattering process, the target photon energy densities and temperatures, the IR with $U_{\rm IR} = 1.2$ eV cm^{-3} and $T_{\rm IR} = 30$ K and the NIR with $U_{\rm NIR} = 20.0$ eV cm^{-3} and $T_{\rm NIR} = 400$ K, are applied (e.g., Torres et al. 2014). By reproducing the multiband observed data, the results show a maximum energy of the electrons and positrons of ~4.6 PeV and a magnetic field strength of ~18.7 μG, which are roughly consistent with Torres et al. (2014) and Lu et al. (2017a). In addition, the radius is ~10.6 pc, which is consistent with the results of the observation.

As shown in Figure 2, the particle cooling and transport processes are analyzed, the particle cooling process is adiabatic loss dominated for $E_e < 9.5 \times 10^6$ MeV energy bands, while synchrotron loss dominates for $E_e > 9.5 \times 10^6$ MeV energy bands. On the other hand, the advection is the most prominent process for $E_e < 8.0 \times 10^8$ MeV energy bands, but the diffusion becomes the dominant process for $E_e > 8.0 \times 10^8$ MeV. In addition, our model gives the current diffusion coefficient $\sim 3.4 \times 10^{26}$ cm^2 s^{-1} at the electron energy of 1 TeV. The spatially radiative properties of MSH 15–52 are investigated by Lu et al. (2017a) using a transport model including the advection and diffusion, whose results indicate the spatial average diffusion coefficient $K = 1.4 \times 10^{25}$ cm^2 s^{-1}. However, the angular radius of radiation region $\theta = 312''$ (the corresponding radius $R \sim 6.6$ pc) is smaller. In addition, the particle diffusion process is assumed to be Bohm-like diffusion. These differences may account for the fact that the diffusion coefficient is smaller than the value estimated by our model.

6. *HESS J1356 − 645*.—The source HESS J1356−645 is powered by PSR J1357−6429 with a 166 ms rotation period, a period derivative of $\dot{P} = 3.6 \times 10^{-13}$ s s^{-1} (e.g., Lorimer et al. 2006), and an unknown braking index, which is assumed to be 3.0. Its distance is estimated to be 2.5 kpc (e.g., Chang et al. 2012). Following Zhu et al. (2018), the age $T_{\rm age} = 6500$ yr. Hence, the initial spin-down timescale $\tau_0 = 810$ yr and the initial luminosity $L_0 = 5.04 \times 10^{38}$ erg s^{-1} are applied.

The multiband observed data are taken from Griffith & Wright (1993), Duncan et al. (1995), and Murphy et al. (2007) (radio band); Abramowski et al. (2011) (X-ray band); Acero et al. (2013) (GeV band); and Abramowski et al. (2011) (TeV band). The TeV images have revealed the radius of the extended source $R_{\rm TeV} = 10.0 \pm 0.9$ pc (e.g., Abdalla et al. 2018). As shown in Figure 1, the multiband nonthermal observed data of the source are reproduced well by synchrotron and IC emission of relativistic electrons and positrons. As seen in Table 1, by the fitting process, the low-energy spectral index $\alpha_1 \sim 1.0$, high-energy spectral index $\alpha_2 \sim 2.56$, and break energy $E_b \sim 5.4 \times 10^4$ MeV are obtained. Some of these values are not consistent with the results of $\alpha_1 \sim 1.2$, $\alpha_2 \sim 2.52$, and $E_b \sim 1.5 \times 10^5$ MeV for Torres et al. (2014). In addition, to reproduce the TeV gamma-ray observation, the target photon energy densities and temperatures, the IR with $U_{\rm IR} = 2.5$ eV cm^{-3} and $T_{\rm IR} = 25$ K and the NIR with $U_{\rm NIR} = 1.2$ eV cm^{-3} and $T_{\rm NIR} = 5000$ K, are applied. These energy densities are larger than what is obtained from the GALPROP code. In fact, the target photon energy densities are generally larger than the values obtained from the GALPROP code based on the position of the source in the Galaxy (usually by up to a factor of a few; e.g., Torres et al. 2014). Our results show a maximum energy of the electrons and positrons of ~1.4 PeV and a magnetic field strength of ~5.7 μG, which are roughly consistent with the magnetic field strength obtained by Torres et al. (2014), 3.5 μG. In addition, the radius is ~10.2 pc, which is consistent with the TeV observation results (e.g., Abdalla et al. 2018).

For the particle transport, the current diffusion coefficient $\sim 1.5 \times 10^{26}$ cm^2 s^{-1} is obtained by our model. In addition, as shown in Figure 2, the particle adiabatic loss dominates the cooling process for $E_e < 6.1 \times 10^7$ MeV energy bands, and synchrotron loss dominates for $E_e > 6.1 \times 10^7$ MeV. On the other hand, the particle transport process is advection dominated, but the diffusion process is important only in the high-energy band.

4. Conclusion and Discussions

In recent years, many studies have found that advection and diffusion play an important role in the particle transport process of PWNe (e.g., Van Etten & Romani 2011; Tang & Chevalier 2012; Vorster & Moraal 2013; Porth et al. 2016; Lu et al. 2017a, 2017b; Ishizaki et al. 2018; H.E.S.S. Collaboration 2019; Lu et al. 2019, 2020; Zhu et al. 2021). However, the previous spatially independent spectrum evolution models of PWNe typically only take diffusion into account and ignore the advection process (e.g., Zhang et al. 2008; Bucciantini et al. 2011; Martin et al. 2012; Torres et al. 2014; Zhu et al. 2018; Fiori et al. 2020, 2022). In this paper, we applied the spectral evolution model involving the advection and diffusion processes to investigate nonthermal radiation properties of six PWNe, G21.5–0.9, Kes 75, G0.9+0.1, MSH 15–52, N157B, and HESS J1356–645. Based on the model, the current multiband observed data of these PWNe are reproduced well (see Figure 1), and the particle cooling and transport processes are investigated (see Figure 2). Our conclusions are summarized as follows:

1. Our results indicate that the fitted parameters for the six PWNe are $1.0 \leqslant \alpha_1 \leqslant 1.7$, $2.3 \leqslant \alpha_2 \leqslant 2.7$, $10^4\,\mathrm{MeV} \leqslant E_b \leqslant 10^6\,\mathrm{MeV}$, $0.002 \leqslant \eta_B \leqslant 0.2$ (which indicates that PWNe are particle dominated), and the radius ratio $\epsilon < 1.0$ (see Table 1). These results are similar to those in previous studies (e.g., Bucciantini et al. 2011; Tanaka & Takahara 2011; Torres et al. 2014; Zhu et al. 2018). In addition, the values of the initial diffusion coefficient $K(t_{\rm ini})$ for the six PWNe lie in the range $3.0 \times 10^{20}\,\mathrm{cm^2\ s^{-1}} < K(t_{\rm ini}) < 4.0 \times 10^{21}\ \mathrm{cm^2\,s^{-1}}$. The reason may be that the turbulence properties are different within different nebulae. It is worth noting that the nature of particle diffusion would strongly depend on the properties of turbulence (e.g., Kolmogorov 1941; Strong et al. 2007; Trotta et al. 2011).

2. The energy band of a particle is divided into three bands based on the ratio $\tau_{\rm syn}/\tau_{\rm ad}$ here. When $\tau_{\rm syn}/\tau_{\rm ad} > 10.0$, the particle cooling process is adiabatic loss dominated; when $0.1 < \tau_{\rm syn}/\tau_{\rm ad} < 10.0$, it is co-dominated by the adiabatic and synchrotron losses; and when $\tau_{\rm syn}/\tau_{\rm ad} < 0.1$, it is dominated by synchrotron loss. Although the division is arbitrary, it is convenient for us to study the particle cooling processes. As shown in the left panel of Figure 2, the adiabatic loss dominates the particle cooling processes in the low-energy band, and the effect of synchrotron losses increases with the increase of energy. Finally, synchrotron loss becomes the most prominent process in the high-energy band.

3. Similar to the particle cooling process, we have defined that the particle transport is advection dominated when $\tau_{\rm diff}/\tau_{\rm adv} > 10.0$; when $0.1 < \tau_{\rm diff}/\tau_{\rm adv} < 10.0$, it is co-dominated by both convection and diffusion; and when $\tau_{\rm diff}/\tau_{\rm adv} < 0.1$, it is dominated by diffusion. As shown in the right panel of Figure 2, the advection dominates the particle transport in the low-energy band, and the effect of diffusion increases with the increase of energy. Lastly, the convection and diffusion co-play prominent roles in the high-energy band.

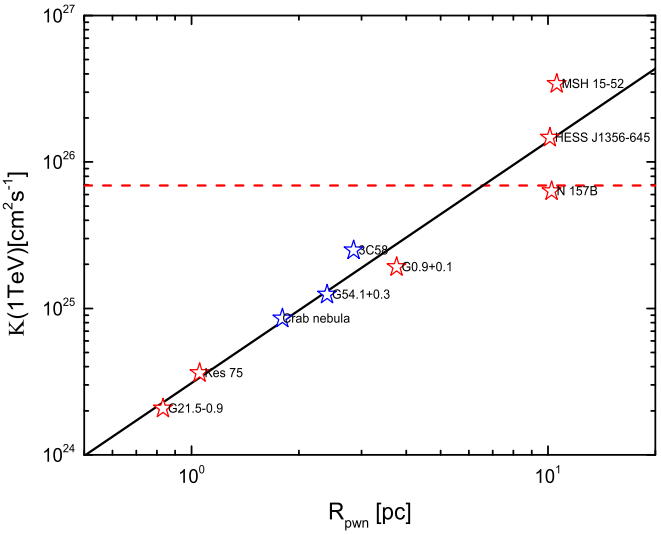

Figure 3. Diffusion coefficients at 1 TeV derived for our sample of six PWNe, and the results of Zhu et al. (2021) for the Crab Nebula, 3C 58, and G54.1 +0.3 are outlined also with blue points. The red dotted lines represent the average value of our samples, and the black line represents the best linear fits $K \propto R_{\rm pwn}^{1.7}$.

4. As shown in Figure 3, there is a variation in the value of the diffusion coefficient of about 2 orders of magnitude (2×10^{24} cm^2 s^{-1} to 3.6×10^{26} cm^2 s^{-1} at the particle energy of 1 TeV) for our sample. In addition, the same model is applied to the Crab Nebula, 3C 58, and G54.1+0.3, and the corresponding diffusion coefficients, e.g., 8.5×10^{24} cm^2 s^{-1}, 2.5×10^{25} cm^2 s^{-1}, and 1.5×10^{25} cm^2 s^{-1}, are obtained in previous work (e.g., Zhu et al. 2021). Here, these three sources are added to the sample, and then we estimated the mean value of the 9 TeV PWN sample to be 6.9×10^{25} cm^2 s^{-1}. Compared with the transport of cosmic rays, the average diffusion coefficient is about 3 orders of magnitude smaller than the value, which is obtained by fits to the AMS-02 boron-to-carbon ratio (B/C) data in the Galaxy (e.g., Genolini et al. 2019). Therefore, we conclude that the slow-diffusion mechanism may exist within PWNe. Unfortunately, the mechanism of the slow diffusion is still unclear. In fact, some studies indicated that the low diffusion mechanism could arise from turbulence owing to the particles themselves (e.g., Yan & Lazarian 2002, 2004; Malkov et al. 2013; Abeysekara et al. 2017; Evoli et al. 2018; Mukhopadhyay & Linden 2022). However, the relativistic turbulence is very intricate so far, which may be caused by the streaming instability of the electrons and positrons released by the center pulsar. Alternatively, the turbulence is generated by the shock wave of the parent SNR (e.g., Fang et al. 2019).

5. The significant correlation between diffusion coefficient and radius of PWNe is found, the result is exhibited in Figure 3, and the best linear fitting result is given by

$$\log K(t) = (24.5 \pm 0.1) + (1.7 \pm 0.2) \log R_{\rm PWN}(t), \quad (21)$$

where $r_{\rm ab} = 0.96$ and $P_{\rm null} \sim 0$. Theoretically, the irregular interaction of particles in the magnetic field will result in diffusion, and it is generally assumed that the diffusion coefficient $K(t) \propto 1/B_{\rm PWN}(t)$ (e.g., Lerche & Schlickeiser 1981; Kennel & Coroniti 1984; Zhang et al. 2008; Vorster & Moraal 2013). In addition, according to the conservation of

magnetic energy, the average magnetic field in the nebula $B_{\rm PWN}(t)$ obeys Equation (15), that is, $B_{\rm pwn}(t) = R_{\rm pwn}^{-2}(t)\left[6\eta_B \int_0^t L(t')R_{\rm pwn}(t')dt'\right]^{0.5}$. As a result, $B_{\rm pwn}(t) \propto R^{-1.5}$, if neglecting the magnetic energy losses due to expansion (e.g., Martin et al. 2012; Torres et al. 2014). On the other hand, $B_{\rm pwn}(t) \propto R^{-2}$ if neglecting the any input from the center pulsar (e.g., Gelfand et al. 2009). Consequently, combined with Equation (13), one gets

$$K(t) \propto R_{\rm PWN}^{\delta}(t), \tag{22}$$

where $1.5 < \delta < 2.0$. In fact, the best-fitting empirical relation $K(t) \propto R_{\rm pwn}^{1.7\pm0.2}$ is consistent with the theoretical result.

We would like to thank the anonymous referee for the very valuable comments. This work is partially supported by the National Natural Science Foundation of China (NSFC 12233006, 11803027) and Yunnan Fundamental Research Projects (grant Nos. 202101AU070099, 202201AT070234).

ORCID iDs

Li Zhang https://orcid.org/0000-0002-7824-4289

References

Abdalla, H., et al. 2018, A&A, 612, A2
Abdo, A. A., Ackermann, M., Ajello, M., et al. 2010, ApJ, 714, 927
Abeysekara, A. U., Albert, A., Alfaro, R., et al. 2017, Sci, 358, 911
Abramowski, A., Acero, F., Aharonian, F., et al. 2011, A&A, 533, A103
Abramowski, A., Acero, F., Aharonian, F., et al. 2012, A&A, 545, L2
Abramowski, A., Aharonian, F., Ait Benkhali, F., et al. 2015, Sci, 347, 406
Acero, F., Ackermann, M., Ajello, M., et al. 2013, ApJ, 773, 77
Aharonian, F., Akhperjanian, A. G., Aye, K. M., et al. 2005a, A&A, 432, L25
Aharonian, F., Akhperjanian, A. G., Aye, K. M., et al. 2005b, A&A, 435, L17
Aharonian, F., et al. 2005c, PhRvL, 126, 241103
Archibald, R. F., Kaspi, V. M., Beardmore, A. P., Gehrels, N., & Kennea, J. A. 2015, ApJ, 810, 67
Arons, J. 2012, SSRv, 173, 341
Arons, J., & Scharlemann, E. T. 1979, ApJ, 231, 854
Atoyan, A. M., & Aharonian, F. A. 1996, MNRAS, 278, 525
Bao, L.-Z., Fang, K., Bi, X.-J., & Wang, S.-H. 2022, ApJ, 936, 183
Bietenholz, M. F., & Bartel, N. 2008, MNRAS, 386, 1411
Blumenthal, G. R., & Gould, R. J. 1970, RvMP, 42, 237
Bock, D. C., & Gaensler, B. M. 2005, ApJ, 626, 343
Bucciantini, N., Arons, J., & Amato, E. 2011, MNRAS, 410, 381
Camilo, F., Ransom, S. M., Gaensler, B. M., et al. 2006, ApJ, 637, 456
Camilo, F., Ransom, S. M., Gaensler, B. M., & Lorimer, D. R. 2009, ApJL, 700, L34
Cao, Z., Aharonian, F. A., An, Q., et al. 2021a, Natur, 594, 33
Cao, Z., Aharonian, F. A., An, Q., et al. 2021b, Sci, 373, 425
Chang, C., Pavlov, G. G., Kargaltsev, O., & Shibanov, Y. A. 2012, ApJ, 744, 81
Chen, Y., Wang, Q. D., Gotthelf, E. V., et al. 2006, ApJ, 651, 237
Cheng, K. S., Cheung, T., Lau, M. M., Yu, K. N., & Kwok, P. W. 1990, JPhG, 16, 1115
De Jager, O. C., Slane, P. O., & LaMassa, S. 2008, ApJL, 689, L125
De Rosa, A., Ubertini, P., Campana, R., et al. 2009, MNRAS, 393, 527
Di Mauro, M., Manconi, S., & Donato, F. 2019, PhRvD, 100, 123015
Di Mauro, M., Manconi, S., & Donato, F. 2020, PhRvD, 101, 103035
Djannati-Atai, A., deJager, O. C., Terrier, R., Gallant, Y. A., & Hoppe, S. 2008, ICRC, 2, 823
Driessen, L. N., Domcek, V., Vink, J., et al. 2018, ApJ, 860, 133
Dubner, G., Giacani, E., & Decourchelle, A. 2008, A&A, 487, 1033
Duncan, A. R., Stewart, R. T., Haynes, R. F., & Jones, K. L. 1995, MNRAS, 277, 36
Evoli, C., Linden, T., & Morlino, G. 2018, PhRvD, 98, 063017
Fang, K., Bi, X.-J., & Yin, P.-F. 2019, MNRAS, 488, 4074
Fang, J., & Zhang, L. 2010, A&A, 515, A20
Feng, J., Tomassetti, N., & Oliva, A. 2016, PhRvD, 94, 123007
Fiori, M., Olmi, B., Amato, E., et al. 2022, MNRAS, 511, 1439
Fiori, M., Zampieri, L., Burtovoi, A., Caraveo, P., & Tibaldo, L. 2020, MNRAS, 499, 3494
Forot, M., Hermsen, W., Renaud, M., et al. 2006, ApJL, 651, L45
Gaensler, B. M., Arons, J., Kaspi, V. M., et al. 2002, ApJ, 569, 878
Gaensler, B. M., Brazier, K. T. S., Manchester, R. N., Johnston, S., & Green, A. J. 1999, MNRAS, 305, 724
Gaensler, B. M., & Slane, P. O. 2006, ARA&A, 44, 17
Gallant, Y. A., & Tuffs, R. J. 1998, MmSAI, 69, 963
Gelfand, J. D., Slane, P. O., & Zhang, W. 2009, ApJ, 703, 2051
Genolini, Y., Boudaud, M., Batista, P. I., et al. 2019, PhRvD, 99, 123028
Giacinti, G., Mitchell, A. M. W., López-Coto, R., et al. 2020, A&A, 636, A113
Gotthelf, E. V., Safi-Harb, S., Straal, S. M., & Gelfand, J. D. 2021, ApJ, 908, 212
Gratton, L. 1972, Ap&SS, 16, 81
Griffith, M. R., & Wright, A. E. 1993, AJ, 105, 1666
Jones, F. C. 1968, PhRv, 167, 1159
Hattori, S., Straal, S. M., Zhang, E., et al. 2020, ApJ, 904, 32
Helfand, D. J., & Becker, R. H. 1987, ApJ, 314, 203
Helfand, D. J., Collins, B. F., & Gotthelf, E. V. 2003, ApJ, 582, 783
H.E.S.S. Collaboration, Abdalla, H., et al. 2019, A&A, 621, A116
Holler, M., et al. 2012, A&A, 539, A24
Horns, D., Aharonian, F., Santangelo, A., Hoffmann, A. I. D., & Masterson, C. 2006, A&A, 451, L51
Hu, C.-P., Ishizaki, W., Ng, C.-Y., Tanaka, S. J., & Mong, Y.-L. 2022, ApJ, 927, 87
Indebetouw, R., et al. 2009, ApJ, 694, 84
Ishizaki, W., Asano, K., & Kawaguchi, K. 2018, ApJ, 867, 141
Kennel, C. F., & Coroniti, F. V. 1984, ApJ, 283, 694
Kolmogorov, A. 1941, DoSSR, 30, 301
Lazendic, J. S., Dickel, J. R., Haynes, R. F., Jones, P. A., & White, G. L. 2000, ApJ, 540, 808
Lerche, I., & Schlickeiser, R. 1981, ApJS, 47, 33
Li, H., Chen, Y., & Zhang, L. 2010, MNRAS, 408, L80
Liu, R. Y., & Yan, H. 2020, MNRAS, 494, 2618
Liu, R. Y., Yan, H., & Zhang, H. 2019, PhRvL, 123, 221103
Livingstone, M. A., Kaspi, V. M., Gavriil, F. P., & Manchester, R. N. 2005, ApJ, 619, 1046
Livingstone, M. A., Kaspi, V. M., Gotthelf, E. V., & Kuiper, L. 2006, ApJ, 647, 1286
Linden, T., Auchettl, K., Bramante, J., et al. 2017, PhRvD, 96, 103016
López-Coto, R., de Oña Wilhelmi, E., Aharonian, F., Amato, E., & Hinton, J. 2022, NatAs, 6, 199
Lorimer, D. R., Faulkner, A. J., Lyne, A. G., et al. 2006, MNRAS, 372, 777
Lu, F. W., Gao, Q. G., & Zhang, L. 2017a, ApJ, 834, 43
Lu, F.-W., Gao, Q.-G., & Zhang, L. 2020, MNRAS, 498, 1911
Lu, F. W., Gao, Q. G., Zhu, B. T., & Zhang, L. 2017b, MNRAS, 472, 2926
Lu, F. W., Gao, Q. G., Zhu, B. T., et al. 2019, A&A, 624, A144
Luo, Y., Lyutikov, M., Temim, T., & Comisso, L. 2020, ApJ, 896, 147
Lyutikov, M., Temim, T., Komissarov, S., et al. 2019, MNRAS, 489, 2403
Malkov, M. A., Diamond, P. H., Sagdeev, R. Z., Aharonian, F. A., & Moskalenko, I. V. 2013, ApJ, 768, 73
Manchester, R. N., Hobbs, G. B., Teoh, A., & Hobbs, M. 2005, AJ, 129, 1993
Marshall, F. E., Gotthelf, E. V., Zhang, W., Middleditch, J., & Wang, Q. D. 1998, ApJL, 499, L179
Martin, J., Torres, D. F., Cillis, A., & de Ona Wilhelmi, E. 2014, MNRAS, 443, 138
Martin, J., Torres, D. F., & Rea, N. 2012, MNRAS, 427, 415
Matheson, H., & Safi-Harb, S. 2010, ApJ, 724, 572
Mereghetti, S., Bandiera, R., Bocchino, F., & Israel, G. L. 2002, ApJ, 574, 873
Mineo, T., Cusumano, G., Maccarone, M. C., et al. 2001, A&A, 380, 695
Mukhopadhyay, P., & Linden, T. 2022, PhRvD, 105, 123008
Murphy, T., Mauch, T., Green, A., et al. 2007, MNRAS, 382, 382
Nynka, M., Hailey, C. J., Reynolds, S. P., et al. 2014, ApJ, 789, 72
Parker, E. N. 1965, P&SS, 13, 9
Porquet, D., Decourchelle, A., & Warwick, R. S. 2003, A&A, 401, 197
Porter, T. A., Moskalenko, I. V., & Strong, A. W. 2006, ApJL, 648, L29
Porth, O., Vorster, M. J., Lyutikov, M., & Engelbrecht, N. E. 2016, MNRAS, 460, 4135
Press, W. H., Teukolsky, S. A., Vetterling, W. T., & Flannery, B. P. 1992, Numerical Recipes in C. The Art of Scientific Computing (Cambridge: Cambridge Univ. Press)
Recchia, S., Di Mauro, M., Aharonian, F. A., et al. 2021, PhRvD, 104, 123017
Rees, M. J., & Gunn, J. E. 1974, MNRAS, 167, 1
Reynolds, S. P., Pavlov, G. G., Kargaltsev, O., et al. 2017, SSRv, 207, 175
Rybicki, G. B., & Lightman, A. P. 1979, Radiative Processes in Astrophysics (New York: Wiley)

Salter, C. J., Reynolds, S. P., Hogg, D. E., Payne, J. M., & Rhodes, P. J. 1989, ApJ, 338, 171
Slane, P. 2017, in Pulsar Wind Nebulae, ed. A. W. Alsabti & P. Murdin (Cham: Springer), 2159
Sidoli, L., Mereghetti, S., Israel, G. L., & Bocchino, F. 2000, A&A, 361, 719
Strong, A. W., Moskalenko, I. V., & Ptuskin, V. S. 2007, ARNPS, 57, 285
Tanaka, S. J., & Takahara, F. 2010, ApJ, 715, 1248
Tanaka, S. J., & Takahara, F. 2011, ApJ, 741, 40
Tang, X., & Chevalier, R. A. 2012, ApJ, 752, 83
Tang, X., & Piran, T. 2019, MNRAS, 484, 3491
Torres, D. F., Cillis, A., Martín, J., & de Oña Wilhelmi, E. 2014, JHEAp, 1, 31
Torres, D. F., & Lin, T. 2018, ApJL, 864, L2
Trotta, R., Jóhannesson, G., Moskalenko, I. V., et al. 2011, ApJ, 729, 106
Tsujimoto, M., Guainazzi, M., Plucinsky, P. P., et al. 2011, A&A, 525, A25
Van Etten, A., & Romani, R. W. 2011, ApJ, 742, 62
van Rensburg, C., Krger, P. P, & Venter, C. 2018, MNRAS, 477, 3853
van Rensburg, C., Venter, C., Seyffert, A. S., & Harding, A. K. 2020, MNRAS, 492, 3091
Venter, C., & de Jager, O. C. 2007, in Proc. of the 363rd WE-Heraeus Seminar on Neutron Stars and Pulsars 40 Years after the Discovery, ed. W. Becker & H. H. Huang (Garching: Max Planck Institut für extraterrestrische Physik), 40
Vorster, M. J., & Moraal, H. 2013, ApJ, 765, 30
Wilson, A. S., & Shakeshaft, J. R. 1972, MNRAS, 160, 355
Yang, X. C., & Zhang, L. 2009, A&A, 496, 751
Yan, H., & Lazarian, A. 2002, PhRvL, 89, 281102
Yan, H., & Lazarian, A. 2004, ApJ, 614, 757
Zhang, L., Chen, S. B., & Fang, J. 2008, ApJ, 676, 1216
Zhang, L., & Yang, X. C. 2009, ApJL, 699, L153
Zhu, B. T., Lu, F. W., Zhou, B., & Zhang, L. 2021, A&A, 655, A41
Zhu, B. T., Zhang, L., & Fang, J. 2018, A&A, 609, A110